

Bayesian Constraints on the Neutron Star Equation of State with a Smooth Hadron–Quark Crossover

Xavier Grundler^{*1} and Bao-An Li^{†1}

¹*Department of Physics and Astronomy, East Texas A&M University, Commerce, TX 75429, USA*

(Dated: February 9, 2026)

We perform a Bayesian inference of the dense-matter equation of state (EOS) within a unified framework that incorporates hadronic matter, quark matter, and a smooth hadron–quark crossover. The EOS is constrained using physical consistency filters, gravitational-wave data from GW170817, NICER mass–radius measurements, and hypothetical future high-precision radius data. We find that current observations strongly constrain the density dependence of the nuclear symmetry energy, particularly its slope and curvature, while the highest-density hadronic parameters and quark-matter parameters remain only weakly constrained. The posterior distributions favor a crossover centered at an energy density $\bar{\varepsilon} \sim (4\text{--}6)\varepsilon_0$ with a width $\Gamma \sim (0.5\text{--}1.0)\varepsilon_0$, where ε_0 is the energy density of symmetric nuclear matter at saturation. The most probable radius of a canonical neutron star is $R_{1.4} \simeq 11.5\text{--}13.0$ km, and the maximum mass is $M_{\text{TOV}} \simeq 2.2 M_{\odot}$. Overall, present data primarily probe the low-to-intermediate density EOS and provide limited direct sensitivity to quark matter and genuinely high-density physics, highlighting the need for next-generation precision radius measurements.

I. INTRODUCTION

Exploring the quantum chromodynamic (QCD) phase diagram is a central problem in both astrophysics and nuclear physics; see, e.g., Refs. [1, 2] for recent reviews. At finite temperature and vanishing baryon density, hadronic matter (HM) is known to undergo a smooth crossover transition to deconfined quark matter (QM) [3]. However, the existence and location of one or more critical endpoints—separating regions of first-order phase transitions from crossover behavior in which the two phases become indistinguishable—remain unknown; see, e.g., Refs. [4–8]. While terrestrial experiments at heavy-ion facilities probe the QCD phase diagram at high temperatures and finite baryon densities up to a few times nuclear saturation density [9, 10], it is not possible to create large volumes of stable, cold, dense nuclear matter in the laboratory. Neutron stars (NS), by contrast, are effectively at zero temperature and can reach central densities of up to six to ten times saturation density, making them unique astrophysical laboratories for exploring the QCD phase diagram in the high-density, low-temperature regime.

In principle, the properties of dense nuclear matter could be derived directly from QCD. In practice, however, lattice QCD is limited to vanishing baryon density, while perturbative QCD is reliable only at asymptotically high densities, far beyond those realized in neutron stars. As a result, a wide range of theoretical approaches have been developed to model the nuclear matter equation of state (EOS), including mean-field theories, effective field theories, Gaussian processes, and phenomenological parameterizations. The EOS, defined as the pres-

sure as a function of energy density, $P(\varepsilon)$, uniquely determines the neutron star mass–radius (MR) relation through the Tolman–Oppenheimer–Volkoff (TOV) equations [11, 12]. Consequently, precise measurements of neutron star masses and radii provide direct constraints on the EOS. In this work, we exploit this connection through a Bayesian analysis informed by modern neutron star observations, including the latest results from the Neutron Star Interior Composition Explorer (NICER).

To construct the EOS, we adopt a phenomenological framework that couples a six-parameter HM meta-model to a two-parameter QM model via a two-parameter smooth crossover function. In many previous studies, including several of our own, the transition between HM and QM has been modeled as a first-order phase transition using either Maxwell or Gibbs constructions; see, e.g., Refs. [13, 14] and references therein. However, lattice QCD results at vanishing baryon density [3], together with implications from recent astrophysical measurements [15], motivate exploring the impact of replacing a sharp first-order transition with a smooth crossover. The role of smooth crossovers in neutron stars has also been investigated in a variety of contexts, including quasinormal modes [16–18], observational signatures [19, 20], peaks in the speed of sound [21, 22], and the emergence of twin-star solutions [23–26]. From a physical perspective, a crossover scenario is supported by the possible percolation of quarks among hadrons at high densities [27–29] or by the existence of quarkyonic matter [30, 31].

In this study, we employ a broad ensemble of EOSs together with a new trace-anomaly-based parameterization for quark matter. Within a Bayesian framework, we infer the most probable values of the EOS parameters and quantify their uncertainties using current neutron star observational data. We place particular emphasis on the squared speed of sound, $c_s^2(\varepsilon)$, and the trace anomaly, defined as $\Delta = 1/3 - P/\varepsilon$, which characterize the stiffness

^{*}xgrundler@leomail.tamuc.edu

[†]Corresponding Author: Bao-An.Li@etamu.edu

of dense matter and the degree of conformal symmetry breaking, respectively. The energy-density dependence of these quantities plays a crucial role in shaping the EOS and has a direct impact on neutron star global properties.

In contrast to most existing Bayesian studies that assume a sharp first-order phase transition, we infer the dense-matter EOS within a unified framework that incorporates a smooth hadron–quark crossover and consistently propagates astrophysical uncertainties across all sectors. This allows us to quantify, in a model-independent manner, how different classes of neutron star observations constrain the speed of sound, the trace anomaly, and the crossover parameters. Our results demonstrate that current measurements primarily constrain the low-to-intermediate density behavior of the symmetry energy, while meaningful inference of quark matter and genuinely high-density physics will require next-generation radius measurements or complementary observables.

The remainder of this paper is organized as follows. In Sec. II, we describe our EOS model and outline the Bayesian methodology. Our main results are presented and discussed in Sec. III. We conclude with a summary and outlook in Sec. IV.

II. METHODS

Below, we describe both the EOS meta-model and the Bayesian framework adopted in this work. The HM EOS employed here is the same as that used in our previous studies [32–45]. Our Bayesian scheme is also closely aligned with these earlier analyses.

A. NS EOS Meta-Model

Our NS EOS consists of four components, three of which are described by meta-models. For the low-density crust, we adopt the Negele–Vautherin (NV) EOS [46] and the Baym–Pethick–Sutherland (BPS) EOS [47] for the inner and outer crusts, respectively. These are connected to the HM core meta-model at the density where the uniform HM EOS becomes thermodynamically unstable, following Refs. [48–50]. Finally, we parameterize a smooth crossover region that interpolates between the HM and QM EOSs. The detailed parameterizations are described in the following subsections. Unless otherwise specified, we use natural units with $c = 1$.

1. HM EOS

The HM meta-model is based on a parameterization of the binding energy per nucleon of β -equilibrated $npe\mu$ matter,

$$E(\rho, \delta) = E_0(\rho) + E_{\text{sym}}(\rho) \delta^2 + \mathcal{O}(\delta^4), \quad (1)$$

where we adopt the empirical isospin-parabolic approximation for neutron-rich matter [51]. Here, ρ denotes the baryon number density and $\delta = (\rho_n - \rho_p)/\rho$ is the isospin asymmetry, with ρ_n and ρ_p being the neutron and proton densities, respectively. The first term, $E_0(\rho)$, is the EOS of symmetric nuclear matter (SNM), while $E_{\text{sym}}(\rho)$ is the nuclear symmetry energy, which quantifies the energy cost of converting protons into neutrons [52].

Both $E_0(\rho)$ and $E_{\text{sym}}(\rho)$ are expanded around the saturation density ρ_0 as

$$E_0(\rho) = E_0(\rho_0) + \frac{K_0}{2} \left(\frac{\rho - \rho_0}{3\rho_0} \right)^2 + \frac{J_0}{6} \left(\frac{\rho - \rho_0}{3\rho_0} \right)^3 \quad (2)$$

$$E_{\text{sym}}(\rho) = E_{\text{sym}}(\rho_0) + L \left(\frac{\rho - \rho_0}{3\rho_0} \right) + \frac{K_{\text{sym}}}{2} \left(\frac{\rho - \rho_0}{3\rho_0} \right)^2 + \frac{J_{\text{sym}}}{6} \left(\frac{\rho - \rho_0}{3\rho_0} \right)^3, \quad (3)$$

where the expansion coefficients are treated as free parameters in the Bayesian analysis. Thus, the series should be viewed as a flexible parameterization rather than a strict Taylor expansion, and convergence at suprasaturation densities is not required. In practice, the highest-order coefficients J_0 and J_{sym} encode the effective contributions from all higher-order terms.

The coefficients are defined by

$$K_0 = 9\rho_0^2 \left. \frac{\partial^2 E_0}{\partial \rho^2} \right|_{\rho_0}, \quad (4)$$

$$J_0 = 27\rho_0^3 \left. \frac{\partial^3 E_0}{\partial \rho^3} \right|_{\rho_0}, \quad (5)$$

$$L = 3\rho_0 \left. \frac{\partial E_{\text{sym}}}{\partial \rho} \right|_{\rho_0}, \quad (6)$$

$$K_{\text{sym}} = 9\rho_0^2 \left. \frac{\partial^2 E_{\text{sym}}}{\partial \rho^2} \right|_{\rho_0}, \quad (7)$$

$$J_{\text{sym}} = 27\rho_0^3 \left. \frac{\partial^3 E_{\text{sym}}}{\partial \rho^3} \right|_{\rho_0}, \quad (8)$$

which correspond to the curvature and skewness of SNM, and the slope, curvature, and skewness of the symmetry energy, respectively, all evaluated at ρ_0 . We fix $\rho_0 = 0.16 \text{ fm}^{-3}$ (the corresponding energy density is $\varepsilon_0 \simeq 150 \text{ MeV/fm}^3$) and $E_0(\rho_0) = -16 \text{ MeV}$, which are well constrained by terrestrial nuclear experiments.

The pressure is obtained from the thermodynamic relation

$$P_{\text{HM}}(\rho, \delta) = \rho^2 \frac{d}{d\rho} \left(\frac{\varepsilon_{\text{HM}}(\rho, \delta)}{\rho} \right), \quad (9)$$

where the HM energy density is $\varepsilon_{\text{HM}}(\rho, \delta) = \rho[E(\rho, \delta) + M_N] + \varepsilon_l(\rho, \delta)$. Here, M_N is the average nucleon mass, and ε_l denotes the lepton energy density, which is calculated using a non-interacting relativistic Fermi gas [12].

2. QM EOS

For the QM meta-model, we adopt the p1 parameterization introduced in Ref. [53], which does not assume a specific microscopic composition of quark matter, such as the presence or absence of strange quarks. This parameterization is formulated in terms of the trace anomaly [19],

$$\Delta \equiv \frac{1}{3} - \frac{P}{\varepsilon}. \quad (10)$$

Following Ref. [53], we parameterize $\Delta(\varepsilon)$ as

$$\Delta = \frac{1}{3} (1 - f t \varepsilon_*^a) e^{-t\varepsilon_*^a}, \quad (11)$$

where t and a are model parameters, and $\varepsilon_* \equiv \varepsilon/\varepsilon_0$. The constant f is fixed to $f = 1.0318$ such that the minimum value of the trace anomaly is $\Delta_{\min} \simeq -0.048$, which represents a lower bound motivated by general relativistic considerations [53]. By construction, this parameterization approaches the conformal limit $c_s^2 \rightarrow 1/3$ as $\varepsilon \rightarrow \infty$, consistent with perturbative QCD expectations [54, 55]. The QM EOS $P_{\text{QM}}(\varepsilon)$ follows directly from the definition of Δ .

In terms of the trace anomaly, the squared speed of sound is given by [19]

$$c_s^2(\varepsilon) \equiv \frac{dP}{d\varepsilon} = -\varepsilon_* \frac{d\Delta}{d\varepsilon_*} + \frac{1}{3} - \Delta, \quad (12)$$

which shows explicitly that, depending on the values of a and t , the parameterization in Eq. (11) can generate a pronounced peak in the sound-speed profile. Such a peak is a common feature of many theoretical models and is often required to sufficiently stiffen the EOS in order to support massive neutron stars consistent with current observations [56–59].

3. Crossover Region

In contrast to much of our previous work, we employ a smooth crossover, rather than a sharp first-order phase transition, to connect the HM and QM EOSs. A variety of interpolation schemes have been proposed in the literature. Common approaches include polynomial interpolations in chemical potential μ [26, 28, 29, 60–63], piecewise-polynomial methods [23, 64], and switching functions based on exponential forms [16, 65–67] or hyperbolic tangent functions [68–71]. The EOS introduced in Ref. [27], for example, employed a hyperbolic tangent function motivated by quark percolation in hadronic matter.

The term “smooth crossover” is used somewhat loosely in the literature. As noted in Ref. [24], it is often applied to any transition other than a Maxwell construction, which features a discontinuity in energy density at fixed pressure. Here, we classify the order of the phase

transition by the continuity properties of the squared speed of sound and its derivatives. Specifically, a discontinuity in $c_s^2(\varepsilon)$ corresponds to a first-order transition, while a discontinuity in its derivative corresponds to a second-order transition. Polynomial interpolations can only enforce smoothness up to a finite order, due to the limited number of adjustable coefficients. To achieve an infinitely differentiable crossover, we therefore adopt a switching function.

Following Ref. [68], the EOS with a crossover is defined as

$$P(\varepsilon) = P_{\text{HM}}(\varepsilon) f_-(\varepsilon) + P_{\text{QM}}(\varepsilon) f_+(\varepsilon), \quad (13)$$

$$f_{\pm}(\varepsilon) = \frac{1}{2} \left[1 \pm \tanh \left(\frac{\varepsilon - \bar{\varepsilon}}{\Gamma} \right) \right], \quad (14)$$

where $\bar{\varepsilon}$ denotes the center of the crossover region and Γ controls its width. This form differs from Ref. [27] in that energy density, rather than baryon number density, is used as the interpolation variable. By construction, the HM EOS dominates for $\varepsilon \lesssim \bar{\varepsilon} - 2\Gamma$, the QM EOS dominates for $\varepsilon \gtrsim \bar{\varepsilon} + 2\Gamma$, and the two are smoothly mixed in between.

The squared speed of sound for the crossover EOS is then given by

$$c_s^2(\varepsilon) = c_{\text{HM}}^2(\varepsilon) f_-(\varepsilon) + P_{\text{HM}}(\varepsilon) \frac{df_-}{d\varepsilon} + c_{\text{QM}}^2(\varepsilon) f_+(\varepsilon) + P_{\text{QM}}(\varepsilon) \frac{df_+}{d\varepsilon}. \quad (15)$$

B. Bayesian Analysis

Bayes’ theorem states that

$$P(\mathcal{M}|D) = \frac{P(D|\mathcal{M}) P(\mathcal{M})}{\int P(D|\mathcal{M}) P(\mathcal{M}) d\mathcal{M}}, \quad (16)$$

which allows us to compute the posterior probability $P(\mathcal{M}|D)$ of a model \mathcal{M} given data D , from the likelihood $P(D|\mathcal{M})$ and the prior $P(\mathcal{M})$. The denominator is a normalization constant (the Bayesian evidence).

Table I: Prior ranges for the EOS parameters.

Parameters	Lower limit	Upper limit
K_0 (MeV)	220	260
J_0 (MeV)	-400	400
$E_{\text{sym}}(\rho_0)$ (MeV)	28.5	34.9
L (MeV)	30	90
K_{sym} (MeV)	-400	100
J_{sym} (MeV)	-200	800
a	0.6	2.42
t	0.025	0.115
$\bar{\varepsilon}$ (MeV)	300	900
Γ (MeV)	5	400

The prior bounds on our model parameters are listed in Table I. For the HM parameters, we sample uniformly

Table II: NICER data with symmetrized uncertainties used to construct bivariate normal likelihoods.

Name	Mass (M_{\odot})	Radius (km)	ρ_{MR}	Model	Analysis
PSR J0740+6620	2.073 ± 0.069	12.49 ± 1.08	0.272	ST-U	Salmi et al. (2024) [72, 73]
PSR J0030+0451	1.40 ± 0.125	11.71 ± 0.855	0.878	ST + PDT	Vinciguerra et al. (2024) [74, 75]
PSR J0437+4715	1.418 ± 0.037	11.36 ± 0.79	0.261	CST + PDT	Choudhury et al. (2024) [76, 77]
PSR J0614+3329	1.44 ± 0.065	10.29 ± 0.935	0.376	ST + PDT	Mauviard et al. (2025) [78, 79]
PSR J1231+1411	1.04 ± 0.04	12.6 ± 0.32	0.0949	PDT-U	Salmi et al. (2024) [80, 81]

and adopt flat priors, treating all values within the specified ranges as equally probable. In previous work, we examined the impact of using Gaussian priors for these parameters and found that the resulting posteriors changed only marginally [82], albeit in a slightly different context. We therefore retain uniform priors here, as they represent the least informative choice.

We adopt the same uniform-prior strategy for the crossover parameters $\bar{\varepsilon}$ and Γ . To our knowledge, no previous studies have systematically explored or constrained prior ranges for these parameters. For comparison, Ref. [68] adopted $\bar{\varepsilon} = 800$ MeV and $\Gamma = 300$ MeV, corresponding to a transition region at several times the saturation density.

For the QM parameters, we employ Gaussian sampling with Gaussian priors centered at $\mu_a = 1.51$ with $\sigma_a = 0.302$, and $\mu_t = 0.07$ with $\sigma_t = 0.014$. These priors are motivated by the analysis of central trace anomalies for 17 NS instances (some of them are for the same NSs but with radii from different measurements or analyses), inferred from their compactness constraints in Ref. [53].

Our likelihood function is defined as

$$P(D|\mathcal{M}) = P_{\text{filter}} \times P_{\text{mass,max}} \times P_R. \quad (17)$$

The first term, P_{filter} , enforces basic physical consistency. EOSs that violate causality are rejected; EOSs that become mechanically unstable are truncated at the point where $dP/d\varepsilon < 0$; and EOSs must yield a positive crust–core transition pressure. In addition to these standard filters used in our previous studies, we impose two further conditions on the crossover region. First, following Ref. [27], we require the crossover region, defined by $\bar{\varepsilon} - 2\Gamma < \varepsilon < \bar{\varepsilon} + 2\Gamma$, to begin above the saturation density, since nuclear matter at saturation is known to be purely hadronic. Second, we require the HM pressure to remain positive throughout the crossover region; although the HM contribution may decrease as the QM component grows, it should not become negative while still contributing to the total EOS.

The factor $P_{\text{mass,max}}$ is a step function enforcing the requirement that the EOS supports a neutron star with mass at least $1.97 M_{\odot}$ [83]. This value represents a conservative lower bound on the maximum nonrotating mass M_{TOV} .

The final term, P_R , incorporates the observational mass–radius data. When the mass is assumed to be

known exactly, we use a univariate Gaussian likelihood,

$$P_R = \prod_{j=1}^N \frac{1}{\sqrt{2\pi}\sigma_{\text{obs},j}} \exp\left[-\frac{(R_{\text{th}} - R_{\text{obs},j})^2}{2\sigma_{\text{obs},j}^2}\right], \quad (18)$$

where R_{th} is the theoretical radius obtained from solving the TOV equations, and $R_{\text{obs},j}$ and $\sigma_{\text{obs},j}$ are the observed radius and uncertainty for the j -th source.

When both mass and radius have observational uncertainties, we adopt a bivariate normal likelihood following Ref. [26],

$$\frac{1}{2\pi\sigma_M\sigma_R\sqrt{1-\rho_{MR}^2}} \exp\left[-\frac{x}{2(1-\rho_{MR}^2)}\right], \quad (19)$$

with

$$x = \frac{(M - \mu_M)^2}{\sigma_M^2} - 2\rho_{MR} \frac{(M - \mu_M)(R - \mu_R)}{\sigma_M\sigma_R} + \frac{(R - \mu_R)^2}{\sigma_R^2}. \quad (20)$$

Here, (M, R) are the theoretical mass–radius pairs from the TOV equations, $(\mu_M, \sigma_M, \mu_R, \sigma_R)$ are the observational values, and ρ_{MR} is the correlation coefficient. For each observation, we evaluate the likelihood at the theoretical point that maximizes Eq. (19), and take the product over all sources.

We consider four observational scenarios:

1. $P_R = 1$: no observational data, which quantifies the constraining power of fundamental physical requirements alone.
2. $R_{1.4} = 11.9 \pm 0.875$ km from the LIGO/Virgo analysis of GW170817 [84], representative of current typical constraints.
3. The most recent NICER measurements summarized in Table II.
4. $R_{1.4} = 11.9 \pm 0.2$ km, corresponding to a hypothetical future measurement with significantly improved precision [85–89].

For PSR J0740+6620 and PSR J0030+0451, multiple NICER analyses exist based on different hotspot models and data selections [90–94]. The choices in Table II are not intended to identify a preferred analysis, but rather to use the most recent results to illustrate the impact of

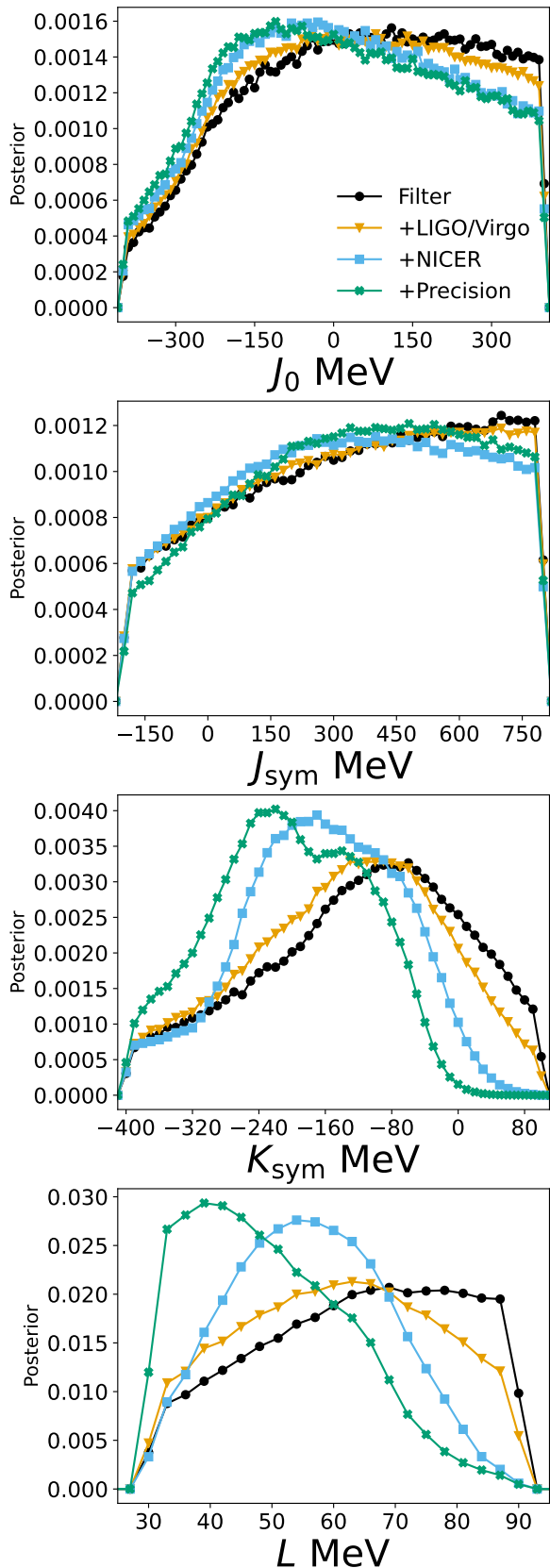


Figure 1: PDFs of the HM parameters.

incorporating multiple observational constraints. Similarly, the results for PSR J1231+1411 are considered less robust due to model convergence issues [80], but are included to provide constraints at low mass and to ensure broad coverage of the mass–radius relation.

To implement the bivariate likelihood, we approximate the asymmetric NICER confidence intervals as Gaussian by averaging the upper and lower 68% bounds to define σ_M and σ_R . The correlation coefficients ρ_{MR} are estimated using the Pearson correlation of the equal-weight posterior samples reported in each analysis.

Posterior probability distributions are obtained using the Metropolis–Hastings algorithm within a Markov Chain Monte Carlo framework. Each chain is evolved for 30,000 burn-in steps, which are discarded, followed by 300,000 production steps used for inference. Most analyses employ eight independent walkers; for the hypothetical high-precision $R_{1.4}$ scenario, we use sixteen walkers to compensate for the lower acceptance rate.

III. RESULTS AND DISCUSSIONS

A. Constraints on the EOS Parameters

Shown in Figs. 1–3 are the marginalized 1-D posterior distribution functions (PDFs) of the EOS parameters.

Beginning with the HM parameters in Fig. 1, we note that two of them are effectively unconstrained by the data. The posterior PDFs of K_0 and $E_0(\rho_0)$ remain essentially identical to their priors. The highest-density parameters for both symmetric nuclear matter and the symmetry energy, J_0 and J_{sym} , are only weakly constrained by the available observations. While very small values of J_0 are disfavored, the posterior distribution exhibits a very broad peak and remains nearly flat toward large values. Since the PDFs of J_0 are almost identical for all likelihood functions considered, we conclude that current radius data provide very limited constraints on J_0 . This conclusion is consistent with results obtained from directly inverting neutron star observables in the J_0 – J_{sym} – K_{sym} parameter space [34].

Physically, J_0 is bounded from above by causality and from below by the requirement that the EOS supports a minimum maximum mass of $M_{\text{TOV}} \gtrsim 1.97 M_{\odot}$ [95]. Since causality provides only a very loose upper bound and realistic EOSs lie well below it, neither the physical filter nor the current radius data significantly constrain the large- J_0 region. On the other hand, the suppression of small J_0 values arises from their direct impact on M_{TOV} , as overly soft EOSs are excluded by the maximum-mass filter.

In the bottom two panels of Fig. 1, we observe substantial differences in the posterior PDFs of L and K_{sym} depending on the astrophysical data included. A modest shift toward softer symmetry energy occurs when the LIGO/Virgo radius information is added to the basic physical filter. This is because, in the absence of explicit

radius constraints, the requirement $M_{\text{TOV}} > 1.97 M_{\odot}$ favors relatively stiff EOSs. It is well known that the radii of canonical neutron stars are primarily determined by the pressure around $2\rho_0$ [48], where the stiffness of matter depends not only on J_0 but also sensitively on L and K_{sym} . The inclusion of LIGO/Virgo data therefore favors slightly softer symmetry energy.

The shift toward smaller values of L and K_{sym} becomes more pronounced when the most recent NICER measurements are used. While PSR J0030+0451 and PSR J0437+4715 are consistent with the LIGO/Virgo results, PSR J0614+3329 exhibits a significantly smaller radius at a comparable mass, implying a softer EOS. Since $R_{1.4}$ is most sensitive to L and K_{sym} [96], it is expected that these parameters are most strongly constrained by radius data. The most dramatic shift occurs when we assume a future high-precision measurement of $R_{1.4} = 11.9 \pm 0.2$ km. In this case, the posterior of L shifts toward its lower bound, and the PDF of K_{sym} develops a dominant peak below -200 MeV, with a secondary peak at larger values. This behavior was also observed in Ref. [41] using mock radius data motivated by proposed next-generation X-ray and gravitational-wave observations [85–89]. The systematic shift toward softer EOSs arises from the highly nonlinear mapping between the EOS and mass–radius relations through the TOV equations [41]. This feature is further verified in Fig. 4 by examining the posterior PDFs of $R_{1.4}$, $R_{2.0}$, and M_{TOV} . The bimodal structure in the PDF of K_{sym} is a consequence of its correlation with both L and J_{sym} [41].

In Fig. 2, we show the posterior PDFs of the QM (also trace anomaly) parameters together with their assumed priors. The parameter t remains fully consistent with its Gaussian prior, while a exhibits only a marginal deviation. The resulting posteriors are nearly identical across all likelihood functions considered, indicating that current neutron star mass–radius data provide essentially no constraints on the QM sector. This implies that present observations do not probe sufficiently deep into the quark-dominated core to extract meaningful information about QM properties, as already pointed out in Ref. [44]. Nevertheless, as we shall discuss below, this result reflects the universal behavior of the dense-matter trace anomaly [97].

Lastly, in Fig. 3, we show the posterior PDFs of the hadron–quark crossover parameters. In contrast to the QM parameters, these distributions differ significantly from their uniform priors. The maximum a posteriori values are approximately $\bar{\varepsilon} \simeq 750$ MeV/fm 3 ($\sim 5\varepsilon_0$) and $\Gamma \simeq 100$ MeV/fm 3 ($\sim 2\varepsilon_0/3$), corresponding to a typical crossover region spanning ~ 550 – 950 MeV/fm 3 .

B. Typical Global Observables

In Fig. 4, we show the posterior probability distributions of three NS global observables: $R_{1.4}$, $R_{2.0}$, and M_{TOV} . If we look at the predicted radii constrained only

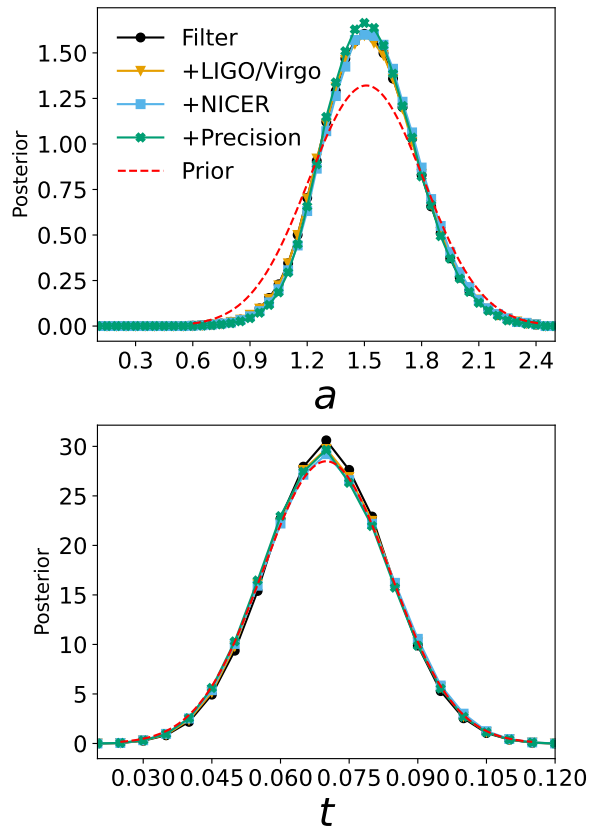


Figure 2: PDFs of the QM parameters.

by basic physics principles included in the filter, we see that $11 \text{ km} \lesssim R_{1.4} \lesssim 14 \text{ km}$ and $10 \text{ km} \lesssim R_{2.0} \lesssim 14 \text{ km}$. The LIGO/Virgo data from GW170817 only slightly favors smaller radii, which is interesting. While the extracted $R_{1.4}$ value for that event was 11.9 ± 0.875 km, our Bayesian inference finds that the most probable value for $R_{1.4}$ is around 12.5 – 12.8 km, still consistent with measurement uncertainty. If we increase the hypothetical precision of the measurement, however, we force $R_{1.4} = 11.9$, requiring a softer EOS as seen in Fig. 1. Using the NICER-informed likelihood, we see $11.5 \text{ km} \lesssim R_{1.4} \lesssim 13.0 \text{ km}$ and $10.5 \text{ km} \lesssim R_{2.0} \lesssim 13 \text{ km}$. This scenario represents the current best set of NS MR constraints.

Looking now at the NS maximum mass M_{TOV} supported by a given EOS, we see that every likelihood used favors $M_{\text{TOV}} \approx 2.2 M_{\odot}$ with slight shifts depending on the exact data used. Ironically, the NICER scenario, despite being the only likelihood informed by a nearly $2.1 M_{\odot}$ NS, does not predict the most massive NS. This behavior reflects the fact that different neutron star observables probe different density regimes of the EOS. While $R_{1.4}$ is primarily sensitive to the pressure around $2\rho_0$, the maximum mass M_{TOV} is determined by the EOS at much higher densities, typically $\gtrsim 4\rho_0$. As a result, an EOS can be relatively soft at intermediate densities,

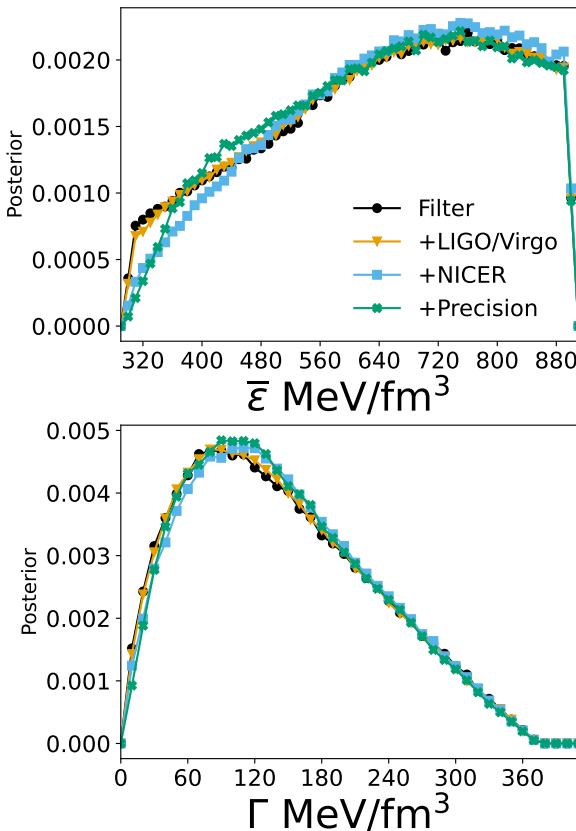


Figure 3: Posterior PDFs of the hadron-quark crossover parameters.

yielding small radii, yet stiffen rapidly at higher densities and support a large maximum mass. In the filter and LIGO/Virgo scenarios, the relatively broad radius constraints still allow such EOSs, leading to posterior distributions of M_{TOV} extending up to $M_{\text{TOV}} \sim 2.6 M_{\odot}$. In contrast, the NICER likelihood constrains radii at multiple masses with smaller uncertainties, effectively requiring the EOS to remain soft over a wider density range. This suppresses the possibility of rapid high-density stiffening and consequently leads to lower inferred values of M_{TOV} , despite the inclusion of a $\sim 2.1 M_{\odot}$ pulsar in the NICER dataset.

C. Energy-Density Profiles of Speed of Sound and Trace Anomaly

We now turn to the behavior of the speed of sound and the trace anomaly in neutron stars as functions of the energy density. In the upper panel of Fig. 5, we show the squared speed-of-sound profile $P(\varepsilon, c_s^2) = N(\varepsilon, c_s^2)/N_{\text{EOS}}$, where $N(\varepsilon, c_s^2)$ is the number of occurrences and N_{EOS} is the total number of EOSs accepted in our Bayesian analysis using the most recent NICER dataset. This quantity represents the probability density of finding matter with

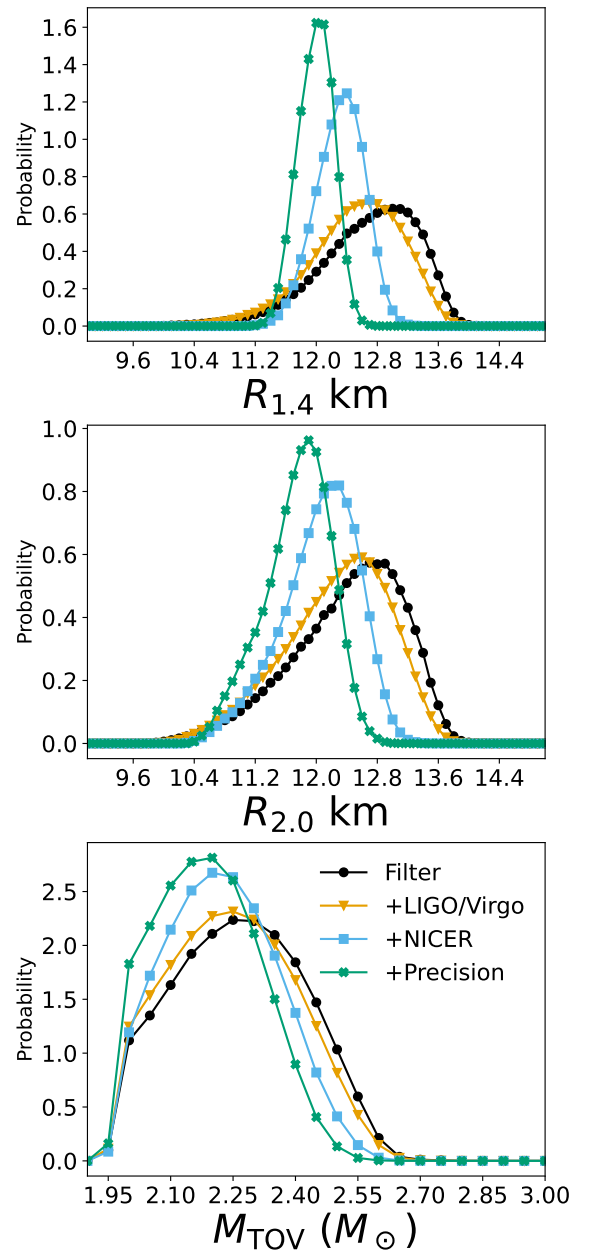


Figure 4: Posterior probability distributions for NS observables $R_{1.4}$ (upper), $R_{2.0}$ (middle), and M_{TOV} (bottom).

a given c_s^2 at a random point inside neutron stars drawn from the accepted EOS ensemble. The lower panel shows the corresponding joint distribution of the trace anomaly $P(\varepsilon, \Delta)$, defined analogously.

These heat maps are joint measures that combine several effects: how frequently a given $c_s^2(\varepsilon)$ or $\Delta(\varepsilon)$ occurs among the EOS ensemble, how much stellar volume is associated with a given energy density, and how many EOSs allow that energy density at all. First of all, it is not surprising that there is a high probability in the low energy density region, but generally lower probabilities at

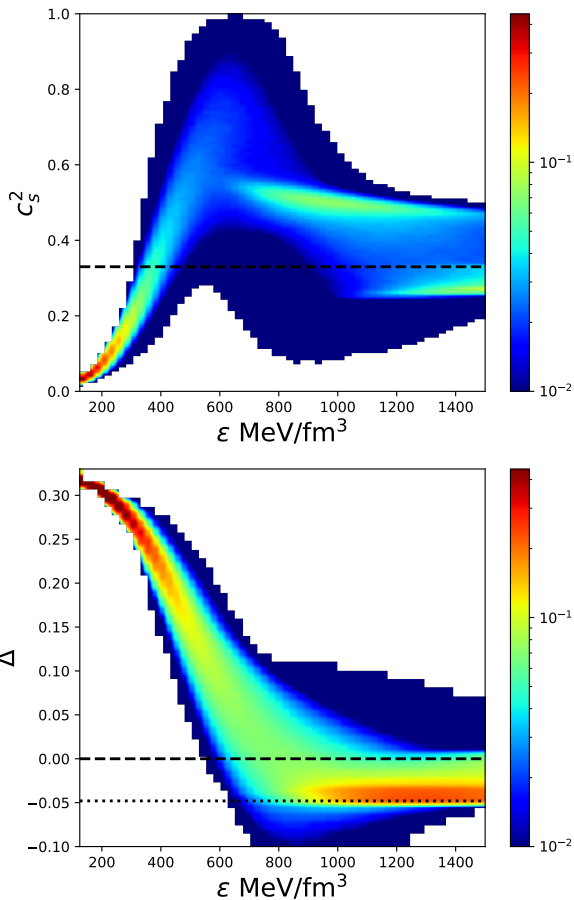


Figure 5: The speed of sound squared and trace anomaly profiles with respect to energy density for accepted EOS using the most recent NICER data. The pQCD conformal limits are indicated by the dashed lines, while the GR limit for the trace anomaly is shown with the dotted line. Every bin was divided by the total number of accepted EOS. Note the logarithmic color scale.

higher energy densities. This is simply because all EOSs selected by our Bayesian analysis have to go through the low energy density region, but not all of them can get into the high energy density regions, only found in the cores of massive NSs. For example, the high probability density at low energy densities, $\varepsilon \lesssim 300$ MeV/fm 3 , which mainly corresponds to the outer regions of all neutron stars, arises from the geometrical $4\pi r^2$ weighting entering the mass integral used during the Bayesian analyses. Toward higher densities in the stellar interior, $c_s^2(\varepsilon)$ generally increases, but the available volume becomes smaller, and few EOSs can support massive NSs where these high energy densities are reached, leading to a reduced probability density.

Interestingly, for EOSs whose central densities lie deep in the post-maximum region of the sound-speed profile, where the EOS undergoes a partial softening associated with the hadron–quark crossover, an extended high-

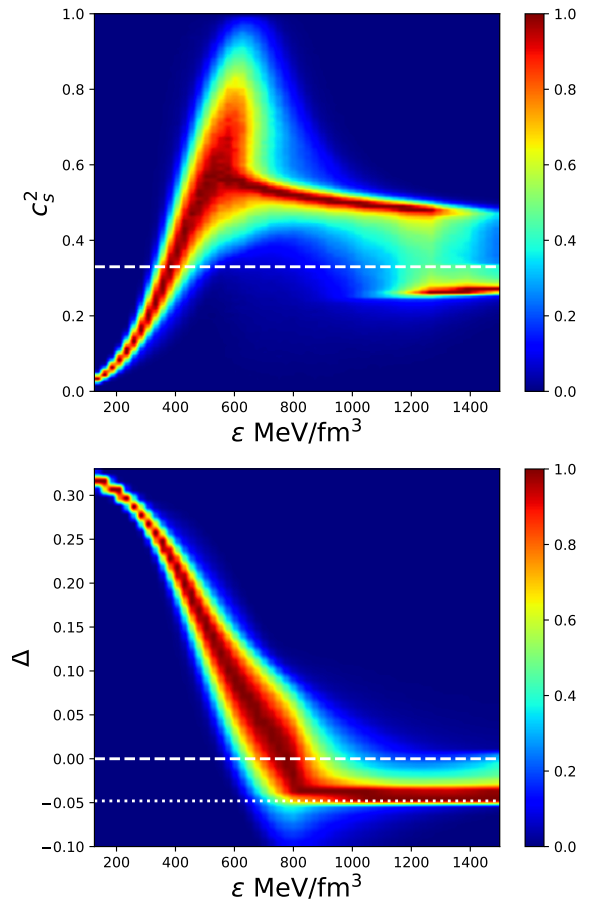


Figure 6: The same as in Fig. 5 but now the count in each energy density bin was scaled to have a maximum value of one.

probability region emerges around $c_s^2 \simeq 0.5$. In addition, a smaller secondary peak appears in the joint distribution near $c_s^2 \simeq 0.25$ and $\varepsilon \simeq 1400$ MeV/fm 3 . For these EOSs, the speed of sound decreases after reaching its maximum and either settles into a lower plateau or asymptotically approaches the general-relativistic bound on the trace anomaly, as shown in the lower panel of Fig. 5.

These secondary structures indicate that a large fraction of the accepted EOSs exhibit similar sound-speed behavior around $\varepsilon \sim 800$ –900 MeV/fm 3 , where they soften toward the quark-matter EOS after the crossover region. This behavior arises because the selected quark-matter EOS is relatively insensitive to the specific parameter choices, leading to a near-universal sound-speed profile in the quark-dominated regime. Consequently, when the stellar central density coincides with these softened segments, a secondary accumulation of probability appears at lower c_s^2 , a phenomenon that is expected to occur preferentially in massive neutron stars, as we shall demonstrate below.

In addition to the globally normalized joint distribution $P(\varepsilon, c_s^2)$, we also show in Fig. 6 an energy-slice–

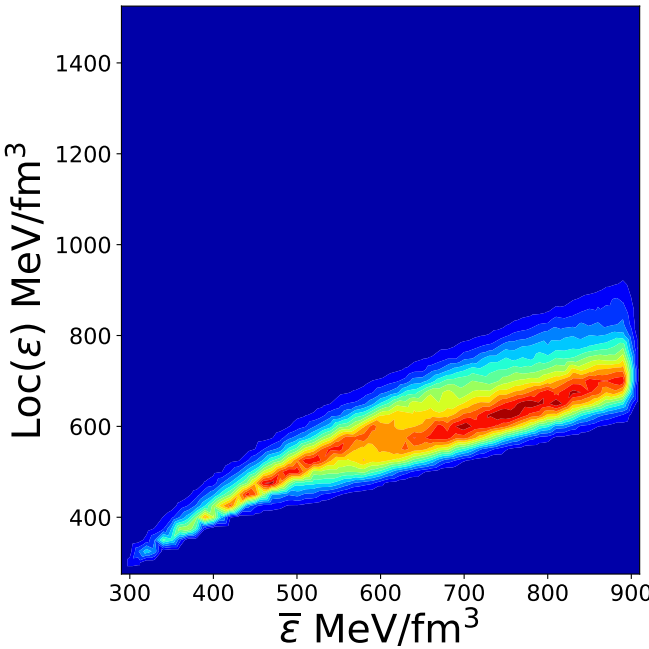


Figure 7: Distribution of pairwise correlation between the central energy density $\bar{\varepsilon}$ of the crossover region and the location $\text{Loc}(\varepsilon)$ in energy density of the maximum speed of sound.

rescaled map in which the maximum count in each ε bin is normalized to unity. This representation does not correspond to a probability density, but rather serves as a contrast-enhanced visualization that highlights the dominant sound-speed branches at fixed energy density and emphasizes EOS-induced structures. Comparing Figs. 5 and 6, we see that the geometrical volume effects are largely removed in the latter, revealing more clearly the crossover-induced ridges and the apparent universality of the sound-speed profile.

It is worth noting that the trace anomaly $\Delta(\varepsilon)$ is confined to a relatively narrow band, whereas the squared speed of sound exhibits much richer structure. This is because $\Delta(\varepsilon) = \frac{1}{3} - \frac{P}{\varepsilon} = \frac{1}{3} - \langle c_s^2(\varepsilon) \rangle$ measures the energy-density-averaged squared speed of sound $\langle c_s^2(\varepsilon) \rangle$ [98, 99],

$$\langle c_s^2(\varepsilon) \rangle = \frac{1}{\varepsilon} \int_0^\varepsilon c_s^2(\varepsilon') d\varepsilon' = \frac{P(\varepsilon)}{\varepsilon}. \quad (21)$$

As shown earlier in Fig. 2, the posterior PDFs of the trace-anomaly parameters t and a are essentially independent of the datasets used, including the high-precision mock radius data, indicating a universal behavior of the dense-matter trace anomaly. This supports the recent finding of Ref. [97] that the trace anomaly serves as a composition-insensitive descriptor of dense matter across widely different physical environments, ranging from heavy-ion collisions to compact stars.

Finally, to assess whether the nonmonotonic behavior of the speed of sound is genuinely induced by the crossover construction rather than being a fine-tuned model artifact, we show in Fig. 7 the pairwise correla-

tion between the crossover parameter $\bar{\varepsilon}$ and the location $\text{Loc}(\varepsilon)$ in energy density of the maximum speed of sound for the accepted EOSs. We find that $\text{Loc}(\varepsilon)$ exhibits a strong, positive, and nearly linear correlation with $\bar{\varepsilon}$. For $\bar{\varepsilon} \lesssim 600 \text{ MeV/fm}^3$, the relation is approximately $\text{Loc}(\varepsilon) \approx \bar{\varepsilon}$, indicating that a smooth crossover naturally induces a peak in the speed of sound within the transition region, consistent with previous studies [27, 100]. For $600 \lesssim \bar{\varepsilon} \lesssim 900 \text{ MeV/fm}^3$, the correlation weakens, which can be attributed to the fact that the hadronic EOS itself may generate a peak in $c_s^2(\varepsilon)$, depending sensitively on the high-density behavior of the nuclear symmetry energy, as demonstrated in Refs. [101, 102] and reviewed in Ref. [103]. In this case, if the crossover sets in at sufficiently high densities, the observed peak in c_s^2 may originate primarily from the hadronic sector.

D. Nonmonotonic Speed-of-Sound Profiles in Massive Neutron Stars

The implications of the features studied above become evident when examining neutron stars of different masses. The top-left panel of Fig. 8 shows the probability distribution of the maximum squared speed of sound, $\max(c_s^2)$, reached by the accepted EOSs. We find that all accepted EOSs violate the conformal bound $c_s^2 < 1/3$. The bottom-left panel shows the corresponding energy density $\text{Loc}(\varepsilon)$ at which $\max(c_s^2)$ occurs. The most probable value is $\text{Loc}(\varepsilon) \simeq 600 \text{ MeV/fm}^3 (\sim 4\varepsilon_0)$, placing it in the early part of the typical crossover region.

In the middle and right panels of Fig. 8, we present the posterior distributions of the central squared speed of sound and central energy density for $1.4 M_\odot$ and $2.0 M_\odot$ neutron stars, respectively. Focusing first on the central energy density, we observe that the most probable value shifts systematically toward higher densities when going from the filter-only case to the LIGO/Virgo, NICER, and precision scenarios. This ordering reflects the corresponding trend from stiffer to softer hadronic EOS parameters, as seen in Fig. 1, and is consistent with the well-known result that stiffer EOSs yield lower central densities at fixed stellar mass [48, 104, 105]. Physically, this behavior follows from the hydrostatic balance governed by the TOV equations: a stiffer EOS provides larger pressure at a given energy density, allowing the star to support its mass at lower central densities, whereas a softer EOS requires higher central densities to achieve equilibrium.

For the central speed of sound in a $1.4 M_\odot$ neutron star, the posterior distribution exhibits a single dominant peak at $c_{s,c,1.4}^2 \simeq 0.5$, essentially independent of the likelihood adopted. For a $2.0 M_\odot$ neutron star, all scenarios display a main peak at $c_{s,c,2.0}^2 \simeq 0.5$ together with a pronounced shoulder extending to larger values, whose detailed shape depends mildly on the specific dataset. This high- c_s^2 shoulder corresponds to EOSs for which the central density of a $2.0 M_\odot$ star lies close to the density

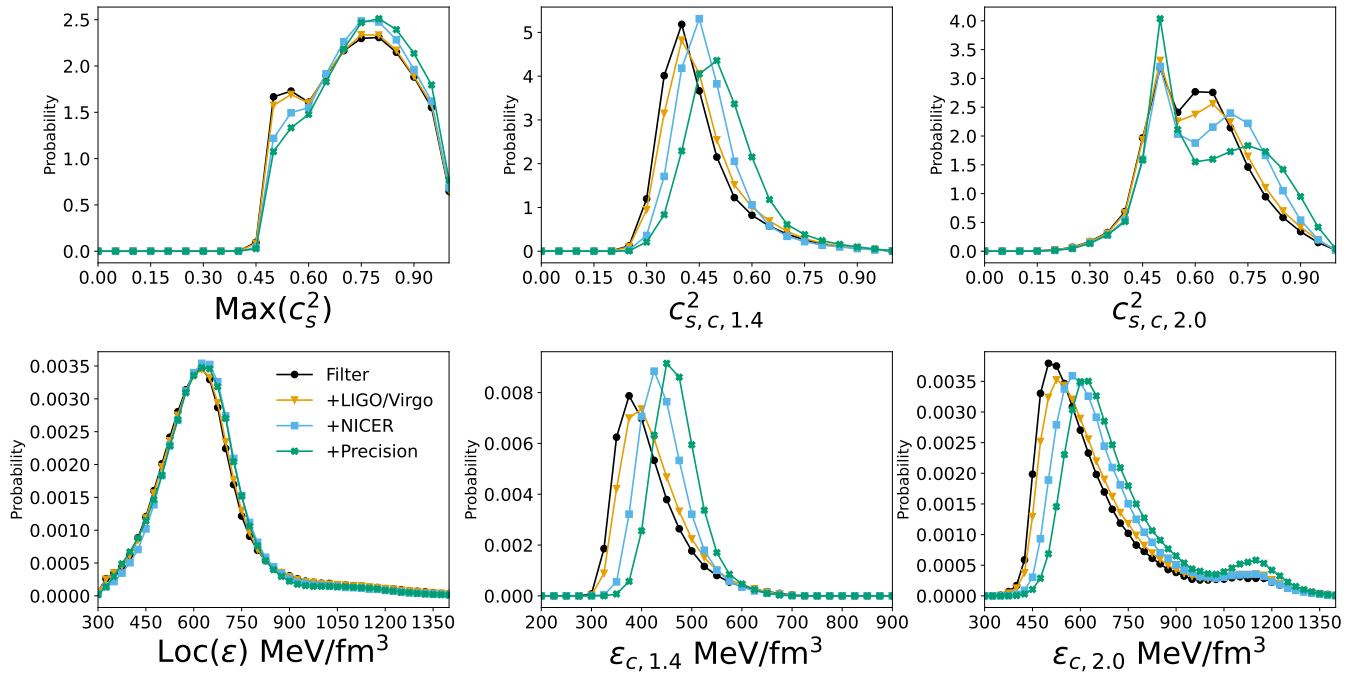


Figure 8: On the left is the probability distribution for the maximum speed of sound squared, $\text{Max}(c_s^2)$, achieved by an EOS (upper panel), and at what energy density, $\text{Loc}(\epsilon)$, it occurs (lower panel). Also shown are the central energy density and speed of sound in canonical neutron stars (middle) and $2.0 M_\odot$ NS (right), respectively. The color and symbol codes are the same as in previous figures.

where the speed of sound reaches its maximum.

At the same time, the distribution of $\epsilon_{c,2.0}$ exhibits a long high-density tail, in which the central density exceeds the location of the peak in c_s^2 . Beyond this point, the speed of sound decreases with increasing energy density. Comparing $\epsilon_{c,2.0}$ with the typical crossover region inferred from Fig. 3, $\epsilon \simeq 550\text{--}950 \text{ MeV/fm}^3$, we find that even $2.0 M_\odot$ neutron stars are, in most cases, located only at the onset of the crossover. Consequently, $1.4 M_\odot$ stars experience essentially no quark-matter effects, while $2.0 M_\odot$ stars probe at most the early crossover regime. This explains why the neutron star observations considered here provide little direct sensitivity to the quark-matter EOS and why the quark-sector parameters remain largely consistent with their priors, as seen in Fig. 2.

IV. SUMMARY AND CONCLUSIONS

In this work, we have performed a Bayesian inference of the dense-matter equation of state within a unified framework that incorporates hadronic matter, quark matter, and a smooth hadron-quark crossover. Using a meta-model description for the hadronic sector, a trace-anomaly-based parameterization for quark matter, and an infinitely differentiable switching function to describe the crossover, we have systematically explored how different classes of neutron star observations constrain the

EOS across a wide range of densities.

We find that current astrophysical data strongly constrain the low-to-intermediate density behavior of the EOS, particularly the slope and curvature of the nuclear symmetry energy. The parameters L and K_{sym} exhibit clear and systematic shifts toward softer values as increasingly precise radius information is incorporated, with the most pronounced constraints emerging in the scenario with hypothetical high-precision measurements of $R_{1.4}$. In contrast, the highest-density hadronic parameters, such as J_0 and J_{sym} , remain only weakly constrained, reflecting the limited sensitivity of present observations to the deepest regions of neutron star interiors.

The quark-matter parameters governing the trace anomaly show essentially no deviation from their assumed Gaussian priors for all likelihood functions considered. This indicates that current mass-radius data do not probe sufficiently deep into the quark-dominated core to extract meaningful information about quark matter properties, consistent with earlier conclusions drawn from hybrid-star analyses. Nevertheless, the universality observed in the posterior behavior of the trace anomaly suggests that its qualitative features may be robust across a broad class of EOS models.

In contrast, the hadron-quark crossover parameters are significantly constrained by the data. The posterior distributions favor a crossover centered at an energy density $\bar{\epsilon} \sim (4\text{--}6)\epsilon_0$ with a width $\Gamma \sim (0.5\text{--}1)\epsilon_0$, correspond-

ing to a transition region spanning roughly $\varepsilon \sim 550\text{--}950 \text{ MeV/fm}^3$. We further find a strong and nearly linear correlation between the crossover center and the energy density at which the speed of sound reaches its maximum, demonstrating that a smooth crossover naturally induces a peak in $c_s^2(\varepsilon)$ within the transition region.

All EOSs accepted in our Bayesian analysis violate the conformal bound $c_s^2 < 1/3$, and the most probable value of the maximum speed of sound occurs at $\varepsilon \sim 4\varepsilon_0$. The central speed of sound in canonical and massive neutron stars peaks around $c_s^2 \simeq 0.5$, with a high- c_s^2 tail for $2.0 M_\odot$ stars corresponding to EOSs whose central densities lie near the location of the sound-speed maximum. These results highlight the important role played by the sound-speed profile and trace anomaly in shaping neutron star global properties.

Overall, our study demonstrates that present neutron star observations primarily constrain the EOS at densities up to a few times nuclear saturation, while quark matter and genuinely high-density physics

remain largely unconstrained. Meaningful inference of the quark sector and the detailed structure of the hadron–quark transition will require next-generation radius measurements with uncertainties at the $\sim 0.2 \text{ km}$ level or complementary observables sensitive to the inner core, such as post-merger gravitational-wave signals or precise moment-of-inertia measurements.

Acknowledgement.— We thank B.J. Cai, W.J. Xie, and N.B. Zhang for helpful discussions. This work was supported in part by the U.S. Department of Energy, Office of Science, under Award No. DE-SC0013702 and NASA-Texas Space Grant Consortium.

DATA AVAILABILITY

All data used in this work are publicly available [106].

[1] S. Bogdanov, et al., in *Snowmass 2021*, Snowmass 2021 Cosmic Frontier White Paper: The Dense Matter Equation of State and QCD Phase Transitions. 2022. arXiv:2209.07412

[2] A. Sorensen, et al., Dense nuclear matter equation of state from heavy-ion collisions. *Prog. Part. Nucl. Phys.* **134**, 104080 (2024). arXiv:2301.13253, doi:10.1016/j.ppnp.2023.104080

[3] K. Fukushima, QCD phase diagram and astrophysical implications. *J. Subat. Part. Cosmol.* **3**, 100066 (2025). arXiv:2501.01907, doi:10.1016/j.jspc.2025.100066

[4] C. Ecker, N. Jokela, M. Järvinen, Locating the QCD critical point with neutron-star observations. arXiv e-prints arXiv:2506.10065 (2025). arXiv:2506.10065, doi:10.48550/arXiv.2506.10065

[5] M. Ferreira, P. Costa, C. Providência, Presence of a critical endpoint in the QCD phase diagram from the net-baryon number fluctuations. *Phys. Rev. D* **98**, 034006 (2018). arXiv:1806.05757, doi:10.1103/PhysRevD.98.034006

[6] M. Stephanov, QCD critical point: Recent developments. *EPJ Web Conf.* **314**, 00042 (2024). arXiv:2410.02861, doi:10.1051/epjconf/202431400042

[7] L. Ferroni, V. Koch, M.B. Pinto, Multiple Critical Points in Effective Quark Models. *Phys. Rev. C* **82**, 055205 (2010). arXiv:1007.4721, doi:10.1103/PhysRevC.82.055205

[8] D. Blaschke, D.E. Alvarez-Castillo, S. Benic, Mass-radius constraints for compact stars and a critical endpoint. *Proc. Sci. CPOD2013*, 063 (2013). arXiv:1310.3803, doi:10.22323/1.185.0063

[9] L. Du, A. Sorensen, M. Stephanov, The QCD phase diagram and Beam Energy Scan physics: A theory overview. *Int. J. Mod. Phys. E* **33**, 2430008 (2024). arXiv:2402.10183, doi:10.1142/9789811294679_0007

[10] J.M. Lattimer, Constraints on Nuclear Symmetry Energy Parameters. Part. *6*, 30–56 (2023). arXiv:2301.03666, doi:10.3390/particles6010003

[11] R.C. Tolman, Static solutions of Einstein’s field equations for spheres of fluid. *Phys. Rev.* **55**, 364–373 (1939). doi:10.1103/PhysRev.55.364

[12] J.R. Oppenheimer, G.M. Volkoff, On massive neutron cores. *Phys. Rev.* **55**, 374–381 (1939). doi:10.1103/PhysRev.55.374

[13] L. Brandes, W. Weise, Constraints on Phase Transitions in Neutron Star Matter. *Symmetry* **16**, 111 (2024). arXiv:2312.11937, doi:10.3390/sym16010111

[14] J.M. Alarcón, E. Lope-Oter, Y. Cano, Effective field theories for neutron stars physics. *Eur. Phys. J. Special Top.* (2025). arXiv:2511.04737, doi:10.1140/epjs/s11734-025-02026-8

[15] L. Brandes, W. Weise, N. Kaiser, Evidence against a strong first-order phase transition in neutron star cores: Impact of new data. *Phys. Rev. D* **108**, 094014 (2023). arXiv:2306.06218, doi:10.1103/PhysRevD.108.094014

[16] C. Constantinou, S. Han, P. Jaikumar, et al., g modes of neutron stars with hadron-to-quark crossover transitions. *Phys. Rev. D* **104**, 123032 (2021). arXiv:2109.14091, doi:10.1103/PhysRevD.104.123032

[17] B.K. Pradhan, D. Chatterjee, D.E. Alvarez-Castillo, Probing hadron–quark phase transition in twin stars using f-modes. *Mon. Not. Roy. Astron. Soc.* **531**, 4640–4655 (2024). arXiv:2309.08775, doi:10.1093/mnras/stae1425

[18] H. Sotani, T. Kojo, Universality in quasinormal modes of neutron stars with quark-hadron crossover. *Phys. Rev. D* **108**, 063004 (2023). arXiv:2308.11494, doi:10.1103/PhysRevD.108.063004

[19] Y. Fujimoto, K. Fukushima, K. Hotokezaka, et al., Signature of hadron-quark crossover in binary-neutron-star mergers. *Phys. Rev. D* **111**, 063054 (2025). arXiv:2408.10298, doi:10.1103/PhysRevD.111.063054

[20] V. Dexheimer, R. Negreiros, S. Schramm, Role of strangeness in hybrid stars and possible observables. *Phys. Rev. C* **91**, 055808 (2015). arXiv:1411.4623, doi:10.1103/PhysRevC.91.055808

[21] H. Tajima, K. Iida, T. Kojo, et al., Tripling Fluctuations and Peaked Sound Speed in Fermionic Matter. *Phys. Rev. Lett.* **135**, 042701 (2025). arXiv:2412.04971, doi:10.1103/4ywp-752m

[22] K. Iida, E. Itou, Velocity of sound beyond the high-density relativistic limit from lattice simulation of dense two-color QCD. *Prog. Theor. Exp. Phys.* **2022**, 111B01 (2022). arXiv:2207.01253, doi:10.1093/ptep/ptac137

[23] A. Ayriyan, N.U. Bastian, D. Blaschke, et al., Robustness of third family solutions for hybrid stars against mixed phase effects. *Phys. Rev. C* **97**, 045802 (2018). arXiv:1711.03926, doi:10.1103/PhysRevC.97.045802

[24] V. Abgaryan, D. Alvarez-Castillo, A. Ayriyan, et al., Two Novel Approaches to the Hadron-Quark Mixed Phase in Compact Stars. *Universe* **4**, 94 (2018). arXiv:1807.08034, doi:10.3390/universe4090094

[25] D.E. Alvarez-Castillo, D. Blaschke, Mixed phase effects on high-mass twin stars. *Phys. Part. Nucl.* **46**, 846–848 (2015). arXiv:1412.8463, doi:10.1134/S1063779615050032

[26] D. Blaschke, A. Ayriyan, D.E. Alvarez-Castillo, et al., Was GW170817 a Canonical Neutron Star Merger? Bayesian Analysis with a Third Family of Compact Stars. *Universe* **6**, 81 (2020). arXiv:2005.02759, doi:10.3390/universe6060081

[27] K. Masuda, T. Hatsuda, T. Takatsuka, Hadron-quark crossover and massive hybrid stars. *PTEP* **2013**, 073D01 (2013). arXiv:1212.6803, doi:10.1093/ptep/ptt045

[28] T. Kojo, P.D. Powell, Y. Song, et al., Phenomenological QCD equation of state for massive neutron stars. *Phys. Rev. D* **91**, 045003 (2015). arXiv:1412.1108, doi:10.1103/PhysRevD.91.045003

[29] J. Takatsy, P. Kovacs, G. Wolf, et al., What neutron stars tell about the hadron-quark phase transition: A Bayesian study. *Phys. Rev. D* **108**, 043002 (2023). arXiv:2303.00013, doi:10.1103/PhysRevD.108.043002

[30] L. McLerran, S. Reddy, Quarkyonic Matter and Neutron Stars. *Phys. Rev. Lett.* **122**, 122701 (2019). arXiv:1811.12503, doi:10.1103/PhysRevLett.122.122701

[31] L. McLerran, A Pedagogical Discussion of Quarkyonic Matter and Its Implication for Neutron Stars. *Acta Phys. Polon. B* **51**, 1067–1077 (2020). doi:10.5506/APhysPolB.51.1067

[32] N.B. Zhang, B.A. Li, J. Xu, Combined constraints on the equation of state of dense neutron-rich matter from terrestrial nuclear experiments and observations of neutron stars. *The Astrophys. J.* **859**, 90 (2018). doi:10.3847/1538-4357/aac027

[33] N.B. Zhang, B.A. Li, Implications of the mass $M = 2.17_{-0.10}^{+0.11} M_{\odot}$ of PSR J0740+6620 on the equation of state of super-dense neutron-rich nuclear matter. *Astrophys. J.* **879**, 99 (2019). arXiv:1904.10998, doi:10.3847/1538-4357/ab24cb

[34] N.B. Zhang, B.A. Li, Impact of NICER’s radius measurement of PSR J0740+6620 on nuclear symmetry energy at suprasaturation densities. *Astrophys. J.* **921**, 111 (2021). arXiv:2105.11031, doi:10.3847/1538-4357/ac1e8c

[35] W.J. Xie, B.A. Li, Bayesian inference of high-density nuclear symmetry energy from radii of canonical neutron stars. *The Astrophys. J.* **883**, 174 (2019). doi:10.3847/1538-4357/ab3f37

[36] W.J. Xie, B.A. Li, Bayesian inference of the symmetry energy of superdense neutron-rich matter from future radius measurements of massive neutron stars. *The Astrophys. J.* **899**, 4 (2020). doi:10.3847/1538-4357/aba271

[37] W.J. Xie, B.A. Li, Bayesian inference of the dense-matter equation of state encapsulating a first-order hadron-quark phase transition from observables of canonical neutron stars. *Phys. Rev. C* **103**, 035802 (2021). arXiv:2009.13653, doi:10.1103/PhysRevC.103.035802

[38] N.B. Zhang, B.A. Li, Properties of first-order hadron-quark phase transition from inverting neutron star observables. *Phys. Rev. C* **108**, 025803 (2023). arXiv:2304.07381, doi:10.1103/PhysRevC.108.025803

[39] N.B. Zhang, B.A. Li, Impact of the nuclear equation of state on the formation of twin stars. *Eur. Phys. J. A* **61**, 31 (2025). arXiv:2406.07396, doi:10.1140/epja/s10050-025-01497-6

[40] W.J. Xie, B.A. Li, N.B. Zhang, Impact of the newly revised gravitational redshift of x-ray burster GS 1826-24 on the equation of state of supradense neutron-rich matter. *Phys. Rev. D* **110**, 043025 (2024). arXiv:2404.01989, doi:10.1103/PhysRevD.110.043025

[41] B.A. Li, X. Grundler, W.J. Xie, et al., Bayesian inference of fine features of the nuclear equation of state from future neutron star radius measurements to 0.1 km accuracy. *Phys. Rev. D* **110**, 103040 (2024). arXiv:2407.07823, doi:10.1103/PhysRevD.110.103040

[42] B.A. Li, P.G. Krastev, D.H. Wen, et al., Towards Understanding Astrophysical Effects of Nuclear Symmetry Energy. *Eur. Phys. J. A* **55**, 117 (2019). arXiv:1905.13175, doi:10.1140/epja/i2019-12780-8

[43] B.A. Li, B.J. Cai, W.J. Xie, et al., Progress in Constraining Nuclear Symmetry Energy Using Neutron Star Observables Since GW170817. *Universe* **7**, 182 (2021). arXiv:2105.04629, doi:10.3390/universe7060182

[44] B.A. Li, X. Grundler, W.J. Xie, et al., Bayesian inference of core properties of hybrid stars from future high-precision measurements of their radii. *The Astrophys. J. press* arXiv:2505.00194 (2026). arXiv:2505.00194, doi:10.48550/arXiv.2505.00194

[45] X. Grundler, B.A. Li, Bayesian quantification of observability and equation of state of twin stars. *Phys. Rev. D* **112**, 103012 (2025). arXiv:2506.13677, doi:10.1103/hsd4-j54y

[46] J.W. Negele, D. Vautherin, Neutron star matter at sub-nuclear densities. *Nucl. Phys. A* **207**, 298–320 (1973). doi:[https://doi.org/10.1016/0375-9474\(73\)90349-7](https://doi.org/10.1016/0375-9474(73)90349-7)

[47] G. Baym, C. Pethick, P. Sutherland, The ground state of matter at high densities: equation of state and stellar models. *The Astrophys. J.* **170**, 299 (1971). doi:10.1086/151216

[48] J. Lattimer, M. Prakash, Neutron star observations: Prognosis for equation of state constraints. *Phys. Reports* **442**, 109–165 (2007). doi:10.1016/j.physrep.2007.02.003

[49] S. Kubis, Nuclear symmetry energy and stability of matter in neutron stars. *Phys. Rev. C* **76**, 025801 (2007). doi:10.1103/PhysRevC.76.025801

[50] J. Xu, L.W. Chen, B.A. Li, et al., Nuclear constraints on properties of neutron star crusts. *The Astrophys. J.* **697**, 1549–1568 (2009). doi:10.1088/0004-637x/697/2/1549

[51] I. Bombaci, U. Lombardo, Asymmetric nuclear mat-

ter equation of state. *Phys. Rev. C* **44**, 1892 (1991). doi:10.1103/PhysRevC.44.1892

[52] B.A. Li, A. Ramos, G. Verde, et al., Topical issue on nuclear symmetry energy. *Eur. Phys. J. A* **50**, 9 (2014). doi:10.1140/epja/i2014-14009-x

[53] B.J. Cai, B.A. Li, Unraveling trace anomaly of supradense matter via neutron star compactness scaling. *Phys. Rev. D* **112**, 023023 (2025). arXiv:2406.05025, doi:10.1103/3p2p-p3d4

[54] R. Somasundaram, I. Tews, J. Margueron, Perturbative QCD and the neutron star equation of state. *Phys. Rev. C* **107**, L052801 (2023). arXiv:2204.14039, doi:10.1103/PhysRevC.107.L052801

[55] D. Zhou, Reexamining constraints on neutron star properties from perturbative QCD. *Phys. Rev. C* **111**, 015810 (2025). arXiv:2307.11125, doi:10.1103/PhysRevC.111.015810

[56] P. Bedaque, A.W. Steiner, Sound velocity bound and neutron stars. *Phys. Rev. Lett.* **114**, 031103 (2015). arXiv:1408.5116, doi:10.1103/PhysRevLett.114.031103

[57] M. Marczenko, Average speed of sound in neutron stars. *Phys. Rev. C* **110**, 045811 (2024). arXiv:2407.15486, doi:10.1103/PhysRevC.110.045811

[58] B.J. Cai, B.A. Li, Z. Zhang, Central speed of sound, the trace anomaly, and observables of neutron stars from a perturbative analysis of scaled Tolman-Oppenheimer-Volkoff equations. *Phys. Rev. D* **108**, 103041 (2023). arXiv:2307.15223, doi:10.1103/PhysRevD.108.103041

[59] B.J. Cai, B.A. Li, Strong gravity extruding peaks in speed of sound profiles of massive neutron stars. *Phys. Rev. D* **109**, 083015 (2024). arXiv:2311.13037, doi:10.1103/PhysRevD.109.083015

[60] G. Baym, T. Hatsuda, T. Kojo, et al., From hadrons to quarks in neutron stars: a review. *Rept. Prog. Phys.* **81**, 056902 (2018). arXiv:1707.04966, doi:10.1088/1361-6633/aaae14

[61] G. Baym, S. Furusawa, T. Hatsuda, et al., New Neutron Star Equation of State with Quark-Hadron Crossover. *Astrophys. J.* **885**, 42 (2019). arXiv:1903.08963, doi:10.3847/1538-4357/ab441e

[62] T. Kojo, G. Baym, T. Hatsuda, Implications of NICER for Neutron Star Matter: The QHC21 Equation of State. *Astrophys. J.* **934**, 46 (2022). arXiv:2111.11919, doi:10.3847/1538-4357/ac7876

[63] T. Minamikawa, T. Kojo, M. Harada, Quark-hadron crossover equations of state for neutron stars: constraining the chiral invariant mass in a parity doublet model. *Phys. Rev. C* **103**, 045205 (2021). arXiv:2011.13684, doi:10.1103/PhysRevC.103.045205

[64] A. Ayriyan, D. Blaschke, A.G. Grunfeld, et al., Bayesian analysis of multimessenger M-R data with interpolated hybrid EoS. *Eur. Phys. J. A* **57**, 318 (2021). arXiv:2102.13485, doi:10.1140/epja/s10050-021-00619-0

[65] A. Lavagno, Hadron-quark crossover phase transition in hybrid compact stars. *Proc. Sci. QNP2024*, 163 (2025). doi:10.22323/1.465.0163

[66] J.I. Kapusta, T. Welle, Neutron stars with a crossover equation of state. *Phys. Rev. C* **104**, L012801 (2021). arXiv:2103.16633, doi:10.1103/PhysRevC.104.L012801

[67] D. Blaschke, E.O. Hanu, S. Liebing, Neutron stars with crossover to color superconducting quark matter. *Phys. Rev. C* **105**, 035804 (2022). arXiv:2112.12145, doi:10.1103/PhysRevC.105.035804

[68] T. Hell, W. Weise, Dense baryonic matter: constraints from recent neutron star observations. *Phys. Rev. C* **90**, 045801 (2014). arXiv:1402.4098, doi:10.1103/PhysRevC.90.045801

[69] Y. Yang, C. Wu, J.F. Yang, Effects of a phase transition in hybrid stars from quark-meson coupling hadronic matter to deconfined quark matter. *Phys. Rev. D* **109**, 063008 (2024). arXiv:2312.08758, doi:10.1103/PhysRevD.109.063008

[70] P. Qin, Z. Bai, S. Wang, et al., Hadron-quark phase transition in neutron star by combining the relativistic Brueckner-Hartree-Fock theory and Dyson-Schwinger equation approach. *Phys. Rev. D* **107**, 103009 (2023). arXiv:2301.02768, doi:10.1103/PhysRevD.107.103009

[71] P. Kovács, J. Takátsy, J. Schaffner-Bielich, et al., Neutron star properties with careful parametrization in the vector and axial-vector meson extended linear sigma model. *Phys. Rev. D* **105**, 103014 (2022). arXiv:2111.06127, doi:10.1103/PhysRevD.105.103014

[72] T. Salmi, et al., The Radius of the High-mass Pulsar PSR J0740+6620 with 3.6 yr of NICER Data. *Astrophys. J.* **974**, 294 (2024). arXiv:2406.14466, doi:10.3847/1538-4357/ad5f1f

[73] T. Salmi, D. Choudhury, Y. Kini, et al., Data and Software for: 'The Radius of the High-mass Pulsar PSR J0740+6620 with 3.6 yr of NICER Data'. (Jun. 2024). doi:10.5281/zenodo.10519473

[74] S. Vinciguerra, et al., An Updated Mass-Radius Analysis of the 2017–2018 NICER Data Set of PSR J0030+0451. *Astrophys. J.* **961**, 62 (2024). arXiv:2308.09469, doi:10.3847/1538-4357/acfb83

[75] S. Vinciguerra, T. Salmi, A.L. Watts, et al., An updated mass-radius analysis of the 2017–2018 NICER data set of PSR J0030+0451. (Nov. 2023). doi:10.5281/zenodo.8239000

[76] D. Choudhury, et al., A NICER View of the Nearest and Brightest Millisecond Pulsar: PSR J0437–4715. *Astrophys. J. Lett.* **971**, L20 (2024). arXiv:2407.06789, doi:10.3847/2041-8213/ad5a6f

[77] D. Choudhury, T. Salmi, S. Vinciguerra, et al., Reproduction package for: 'A NICER View of the Nearest and Brightest Millisecond Pulsar: PSR J0437–4715'. (Aug. 2024). doi:10.5281/zenodo.13766753

[78] L. Mauviard, S. Guillot, T. Salmi, et al., A NICER view of the 1.4 solar-mass edge-on pulsar PSR J0614–3329. *arXiv e-prints* arXiv:2506.14883 (2025). arXiv:2506.14883, doi:10.48550/arXiv.2506.14883

[79] L. Mauviard, S. Guillot, T. Salmi, et al., Data and Reproduction package for: 'A NICER view of the 1.4 solar-mass edge-on pulsar PSR J0614–3329'. (Oct. 2025). doi:10.5281/zenodo.17380576

[80] T. Salmi, et al., A NICER View of PSR J1231–1411: A Complex Case. *Astrophys. J.* **976**, 58 (2024). arXiv:2409.14923, doi:10.3847/1538-4357/ad81d2

[81] T. Salmi, J. Deneva, P.S. Ray, et al., Data and Software for: 'A NICER View of PSR J1231-1411: A Complex Case'. (Sep. 2024). doi:10.5281/zenodo.13358349

[82] W.J. Xie, B.A. Li, Bayesian inference of the incompressibility, skewness and kurtosis of nuclear matter from empirical pressures in relativistic heavy-ion collisions. *J. Phys. G* **48**, 025110 (2021). arXiv:2001.03669, doi:10.1088/1361-6471/abd25a

[83] J. Antoniadis, et al., A Massive Pulsar in a Compact Relativistic Binary. *Sci.* **340**, 6131 (2013).

arXiv:1304.6875, doi:10.1126/science.1233232

[84] B.P. Abbott, et al., GW170817: Measurements of neutron star radii and equation of state. *Phys. Rev. Lett.* **121**, 161101 (2018). doi:10.1103/PhysRevLett.121.161101

[85] K. Chatzioannou, Uncertainty limits on neutron star radius measurements with gravitational waves. *Phys. Rev. D* **105**, 084021 (2022). arXiv:2108.12368, doi:10.1103/PhysRevD.105.084021

[86] C. Pacilio, A. Maselli, M. Fasano, et al., Ranking love numbers for the neutron star equation of state: The need for third-generation detectors. *Phys. Rev. Lett.* **128**, 101101 (2022). arXiv:2104.10035, doi:10.1103/PhysRevLett.128.101101

[87] A. Bandopadhyay, K. Kacanja, R. Somasundaram, et al., Measuring neutron star radius with second and third generation gravitational wave detector networks. *Cl. Quant. Grav.* **41**, 225003 (2024). arXiv:2402.05056, doi:10.1088/1361-6382/ad828a

[88] D. Finstad, L.V. White, D.A. Brown, Prospects for a precise equation of state measurement from Advanced LIGO and Cosmic Explorer. *Astrophys. J.* **955**, 45 (2023). arXiv:2211.01396, doi:10.3847/1538-4357/acf12f

[89] K. Walker, R. Smith, E. Thrane, et al., Precision constraints on the neutron star equation of state with third-generation gravitational-wave observatories. *Phys. Rev. D* **110**, 043013 (2024). arXiv:2401.02604, doi:10.1103/PhysRevD.110.043013

[90] T.E. Riley, et al., A NICER View of the Massive Pulsar PSR J0740+6620 Informed by Radio Timing and XMM-Newton Spectroscopy. *Astrophys. J. Lett.* **918**, L27 (2021). arXiv:2105.06980, doi:10.3847/2041-8213/ac0a81

[91] M.C. Miller, et al., The Radius of PSR J0740+6620 from NICER and XMM-Newton Data. *Astrophys. J. Lett.* **918**, L28 (2021). arXiv:2105.06979, doi:10.3847/2041-8213/ac089b

[92] A.J. Dittmann, et al., A More Precise Measurement of the Radius of PSR J0740+6620 Using Updated NICER Data. *Astrophys. J.* **974**, 295 (2024). arXiv:2406.14467, doi:10.3847/1538-4357/ad5f1e

[93] T.E. Riley, et al., A NICER View of PSR J0030+0451: Millisecond Pulsar Parameter Estimation. *Astrophys. J. Lett.* **887**, L21 (2019). arXiv:1912.05702, doi:10.3847/2041-8213/ab481c

[94] M.C. Miller, et al., PSR J0030+0451 Mass and Radius from NICER Data and Implications for the Properties of Neutron Star Matter. *Astrophys. J. Lett.* **887**, L24 (2019). arXiv:1912.05705, doi:10.3847/2041-8213/ab50c5

[95] N.B. Zhang, B.A. Li, Extracting Nuclear Symmetry Energies at High Densities from Observations of Neutron Stars and Gravitational Waves. *Eur. Phys. J. A* **55**, 39 (2019). arXiv:1807.07698, doi:10.1140/epja/i2019-12700-0

[96] J. Richter, B.A. Li, Empirical radius formulas for canonical neutron stars from bidirectionally selecting features of equations of state in extended Bayesian analyses of observational data. *Phys. Rev. C* **108**, 055803 (2023). arXiv:2307.05848, doi:10.1103/PhysRevC.108.055803

[97] B.A. Li, Universal Dense-Matter Trace Anomaly Inferred from Collective Flow in Heavy-Ion Collisions and Global Properties of Neutron Stars. to be published. arXiv:2601.13374

[98] J.A. Saes, R.F.P. Mendes, N. Yunes, Approximately universal I-Love- $\langle cs^2 \rangle$ relations for the average neutron star stiffness. *Phys. Rev. D* **110**, 024011 (2024). arXiv:2402.05997, doi:10.1103/PhysRevD.110.024011

[99] M. Marczenko, Average speed of sound in neutron stars. *Phys. Rev. C* **110**, 045811 (2024). arXiv:2407.15486, doi:10.1103/PhysRevC.110.045811

[100] Y.J. Huang, L. Baiotti, T. Kojo, et al., Merger and Postmerger of Binary Neutron Stars with a Quark-Hadron Crossover Equation of State. *Phys. Rev. Lett.* **129**, 181101 (2022). arXiv:2203.04528, doi:10.1103/PhysRevLett.129.181101

[101] N.B. Zhang, B.A. Li, Impact of symmetry energy on sound speed and spinodal decomposition in dense neutron-rich matter. *Eur. Phys. J. A* **59**, 86 (2023). arXiv:2208.00321, doi:10.1140/epja/s10050-023-01010-x

[102] J.T. Ye, R. Wang, S.P. Wang, et al., High-density Symmetry Energy: A Key to the Solution of the Hyperon Puzzle. *Astrophys. J.* **985**, 238 (2025). arXiv:2411.18349, doi:10.3847/1538-4357/addr017

[103] B.A. Li, Beyond $\rho^{2/3}$ Scaling: Microscopic Origins and Multimessengers of High-Density Nuclear Symmetry Energy. *Eur. Phys. Jour. Special Top. on Probing Dense Nucl. Matter*. doi:10.1140/epjs/s11734-026-02124-1

[104] J.M. Lattimer, The nuclear equation of state and neutron star masses. *Ann. Rev. Nucl. Part. Sci.* **62**, 485–515 (2012). arXiv:1305.3510, doi:10.1146/annurev-nucl-102711-095018

[105] F. Özel, P. Freire, Masses, Radii, and the Equation of State of Neutron Stars. *Ann. Rev. Astron. Astrophys.* **54**, 401–440 (2016). arXiv:1603.02698, doi:10.1146/annurev-astro-081915-023322

[106] X. Grundler, B.A. Li, Bayesian quantification of observability and underlying equation of state of twin stars. doi:10.7910/DVN/VWG4N1